ADVANCED FUNCTIONAL MATERIALS
www.afm-journal.de

www.MaterialsViews.com

Design of Hybrid MnO_2-Polymer-Lipid Nanoparticles with Tunable Oxygen Generation Rates and Tumor Accumulation for Cancer Treatment

*Claudia R. Gordijo, Azhar Z. Abbasi, Mohammad Ali Amini, Ho Yin Lip, Azusa Maeda, Ping Cai, Peter J. O'Brien, Ralph S. DaCosta, Andrew M. Rauth, and Xiao Yu Wu**

Manganese dioxide (MnO_2) nanoparticles (NPs) were discovered in previous work to be effective in improving tumor oxygenation (hypoxia) and reducing H_2O_2 and acidity in the tumor microenvironment (TME) via local injection. To develop MnO_2 formulations useful for clinical application, hybrid NPs are designed with tailored hydrophobicity and structure suitable for intravenous injection, with good blood circulation, biocompatibility, high tumor accumulation, and programmable oxygen generation rate. Two different hybrid NPs are constructed by embedding polyelectrolyte-MnO_2 (PMD) in hydrophilic terpolymer/protein-MnO_2 (TMD) or hydrophobic polymer/lipid-MnO_2 (LMD) matrices. The in vitro reactivity of the MnO_2 toward H_2O_2 is controlled by matrix material and NP structure and dependent on pH with up to two-fold higher O_2 generation rate at acidic (tumor) pH than at systemic pH. The hybrid NPs are found to be safe to cells in vitro and organs in vivo and effectively decrease tumor hypoxia and hypoxia-inducible-factor-1alpha through local or systemic administration. Fast acting TMD reduces tumor hypoxia by 70% in 0.5 h by local injection. Slow acting LMD exhibits superior tumor accumulation and retention through the systemic administration and decreased hypoxia by 45%. These findings encourage a broader use of hybrid MD NPs to overcome TME factors for cancer treatment.

1. Introduction

Hypoxia (lack of oxygen) is a common characteristic of the tumor microenvironment (TME) and a negative clinical prognostic factor for a variety of solid tumors due to its critical role in tumor progression, metastasis, and resistance to mainline treatments.[1] Tumor hypoxia is at least partially responsible for the stabilization of hypoxia-inducible-factor-1alpha (HIF-1α), a transcription factor that switches on a cascade of harmful gene and protein expression and metabolic changes in the tumor.[2–4] The metabolic changes driven by hypoxia promote acidosis (acidic pH in the tumor) and increased rates of reactive oxygen species (ROS) production contributing to an even more abnormal TME.[4,5] The multifactorial nature of the TME remains a major challenge for the treatment of solid tumors and recurrent and metastatic cancers.[1,2] Several approaches have been investigated to specifically target individual TME factors to improve treatment outcome,[6] particularly in combination with radiation therapy (RT).[7] However, many previous approaches have not achieved clinical success due to safety issues and inconsistent response. Moreover, treatments such as antiangiogenic therapy can increase hypoxia in the tumor.[8]

Having realized that multiple factors, e.g., hypoxia, acidosis, and ROS, must be dealt with as a whole in order to normalize the TME, we explored the utility of MnO_2 nanoparticles (NPs) for simultaneous modulation of these multiple factors in the TME.[9] Oxo-compounds of manganese (e.g., MnO_2) are among the strongest oxidants found naturally in the environment.[10] Colloidal MnO_2 shows high specificity and reactivity toward H_2O_2 producing O_2 and H_2O, while consuming protons in the reaction.[9] One important feature of this system is that the reaction between MnO_2 NPs and H_2O_2 is not purely catalytic and can lead to the breakdown of the MnO_2 to harmless Mn^{2+} ions, likely depending on the pH.[9,11,12] This characteristic can be particularly useful for biological applications where the breakdown and clearance of the NP is highly desirable to avoid toxicity caused by NP accumulation in the body.[13] Also, in contrast to other metal and metal oxides with peroxidase activity, MnO_2 catalyzes the decomposition of H_2O_2 without generation of highly reactive hydroxyl radicals.[14]

Dr. C. R. Gordijo, Dr. A. Z. Abbasi, M. A. Amini, H. Y. Lip, Dr. P. Cai, Prof. P. J. O'Brien, Prof. X. Y. Wu
Leslie Dan Faculty of Pharmacy
University of Toronto
Toronto, ON, M5S 3M2, Canada
E-mail: xywu@phm.utoronto.ca

A. Maeda, Dr. R. S. DaCosta, Prof. A. M. Rauth
Department of Medical Biophysics
University of Toronto
Toronto, ON, M5G 2M9, Canada

Prof. P. J. O'Brien
Department of Pharmacology and Toxicology
Faculty of Medicine
University of Toronto
Toronto, ON, M5S 1A8, Canada

Dr. R. S. DaCosta
Princess Margaret Cancer Center
The Campbell Family Institute for Cancer Research
University Health Network
Toronto, ON, M5G 1L7, Canada

Dr. R. S. DaCosta
Techna Institute
University Health Network
Toronto ON, M5G 1P5, Canada

DOI: 10.1002/adfm.201404511

Envisioning the usefulness of the MnO_2-catalyzed H_2O_2 decomposition and proton consumption for the modulation of multiple TME factors, we have previously developed injectable, biocompatible albumin-conjugated MnO_2 NPs (AMD NPs) and demonstrated their multifunctionality in modulating the TME.[9] This first generation of MnO_2 NPs exhibited three simultaneous effects on the TME: (1) reduction of ROS levels by reacting with endogenous H_2O_2 produced in excess by cancer cells, (2) reduction of hypoxia by generating measurable amounts of O_2 in situ, and (3) reduction of acidosis by consuming protons during the reaction. AMD NPs injected into tumors decreased tumor hypoxia and acidosis in vivo, as well as resulted in a sustainable down-regulation of HIF-1α and vascular endothelial growth factor (VEGF), a downstream target of HIF-1 that promotes angiogenesis.[9] Our proof-of-concept data also showed that the combination of AMD NPs with a single dose of RT increased tumor cell kill and delayed tumor growth significantly more than RT alone, possibly due to in situ generation of O_2 sensitizing hypoxic cells to ionizing radiation.[9] This was the first demonstration that an injectable NP system was able to manipulate the TME "assembly" as well as enhance RT. Moreover, for the first time MnO_2, a material that has been almost exclusively limited to applications in batteries, sensors, and implantable devices,[11,12,15] was shown to be a potentially powerful new element in nanomedicine, particularly for cancer therapy.

These compelling results suggest the use of MnO_2 as an effective and safe method to modulate the TME and overcome TME-mediated tumor resistance to therapies. However, owing to the small size, unknown colloidal stability in the blood circulation, and uncontrollable reactivity and consequent fast consumption of the MnO_2, the use of AMD NPs has been limited to local intratumoral (IT) injection. To develop a MnO_2 NP formulation useful for clinical application, its suitability for intravenous (IV) injection (systemic administration), good systemic circulation and biocompatibility, effective tumor accumulation, and programmable oxygen generation rate must be considered. Therefore, in this work, we focused on the design of hybrid MnO_2 NPs able to fulfill the above requirements by manipulating material properties and NP structures.[16] We hypothesize that by tailoring material hydrophobicity and NP structure, the reactivity of the MnO_2 can be modulated to tune O_2 generation rate for local or systemic administration, and to provide a higher O_2 generation rate in the TME than in the systemic circulation. The latter feature is vital to ensure that the MnO_2 content of the NPs is not completely consumed by reaction with H_2O_2 levels in the blood circulation prior to reaching the tumor. We have chosen biocompatible polymers and lipids with various hydrophobicities as carrier materials. A graft terpolymer (poly(methacrylic acid)-polysorbate 80-starch) (TER), created by Wu and co-workers and successfully used for making hybrid NP systems for imaging and cancer drug delivery[17] was used in combination with bovine serum albumin (BSA) and polyethylene glycol (PEG) for preparation of terpolymer/protein hydrophilic matrix-based NPs. Solid lipid (myristic acid) and PEG,[18,19] demonstrated useful for preparing NP systems with imaging agents and chemotherapeutics, were selected for preparation of an hydrophobic polymer/lipid matrix.[19] The materials selected for both matrices are pharmaceutically acceptable, and NPs made from them have also shown high passive accumulation in tumors via the enhanced permeability and retention (EPR) effect.[17,19]

The properties of these materials were exploited to engineer two new generations of clinically acceptable MnO_2-containing NPs for both local and systemic administrations. We aimed to make NPs with tunable oxygen generation rates that exhibit higher reactivity toward H_2O_2 in the acidic TME than in the systemic circulation or in normal tissue with higher pH. The surface of both types of hybrid NPs was modified with PEG corona for prolonged circulation in the blood. The effects of NP structure and the medium pH on the reactivity of the MnO_2 contained in these NPs toward H_2O_2 were evaluated. The in vitro biocompatibility, in vivo organ toxicity, and in vivo effect of the hybrid NPs on the modulation of tumor hypoxia and HIF-1α were investigated.

2. Results and Discussion

2.1. Hybrid NPs Made with Varying Hydrophobicity and Structure

Previous work suggested that small albumin-conjugated MnO_2 NPs reacted quickly with H_2O_2, which could limit their application when administered systemically.[9] In this work we developed hybrid MnO_2 NPs with varying hydrophobicity and structure to tune the reaction rate. This was based on the hypothesis that hydrophobicity and structure of the matrix would influence the rates of H_2O_2 and O_2 diffusion in the particle, as well as the surface of MnO_2 NPs exposed to reactants (i.e., H_2O_2 and H^+). Tailoring the carrier hydrophobicity and structure was expected to modulate the reactivity of the MnO_2 for O_2 generation by providing a barrier to diffusion of H_2O_2 from outside the particle to reach the inner reactive MnO_2 sites, thus slowing O_2 generation under physiological (pH 7.4) conditions. Herein we prepared precursor polyelectrolyte-MnO_2 (PMD) NPs, by closely following our previously established protocol,[9] and embedded them in hydrophilic terpolymer/protein or hydrophobic polymer/lipid matrices. We selected hydrophilic terpolymer (Figure SI.1, Supporting Information) and hydrophobic myristic acid as carrier materials of the PMD due to the high colloidal stability and superior tumor accumulation of NPs made from these materials.[17,19]

Hydrophilic terpolymer-MnO_2 hybrid NPs (TMD) were obtained by successfully loading PMD in denatured BSA crosslinked with terpolymer. As summarized in **Figure 1**a, TMD was prepared by mixing PMD with BSA to form a PMD/BSA complex.[9] The protein/PMD complex was denatured by sonication and heating and crosslinked with terpolymer through the covalent conjugation of the amino groups of the BSA with the carboxylic groups of TER. To obtain TMD functionalized with PEG molecules, a mixture of polyoxyethylene stearate (lipid-PEG) of different $\bar{M}_w$ (2 and 5 kDa) was added during NP preparation.

Hydrophobic myristic acid-MnO_2 hybrid NPs (LMD) were obtained by loading PMD in solid lipid NPs of myristic acid, as represented in Figure 1b. For effective loading into the

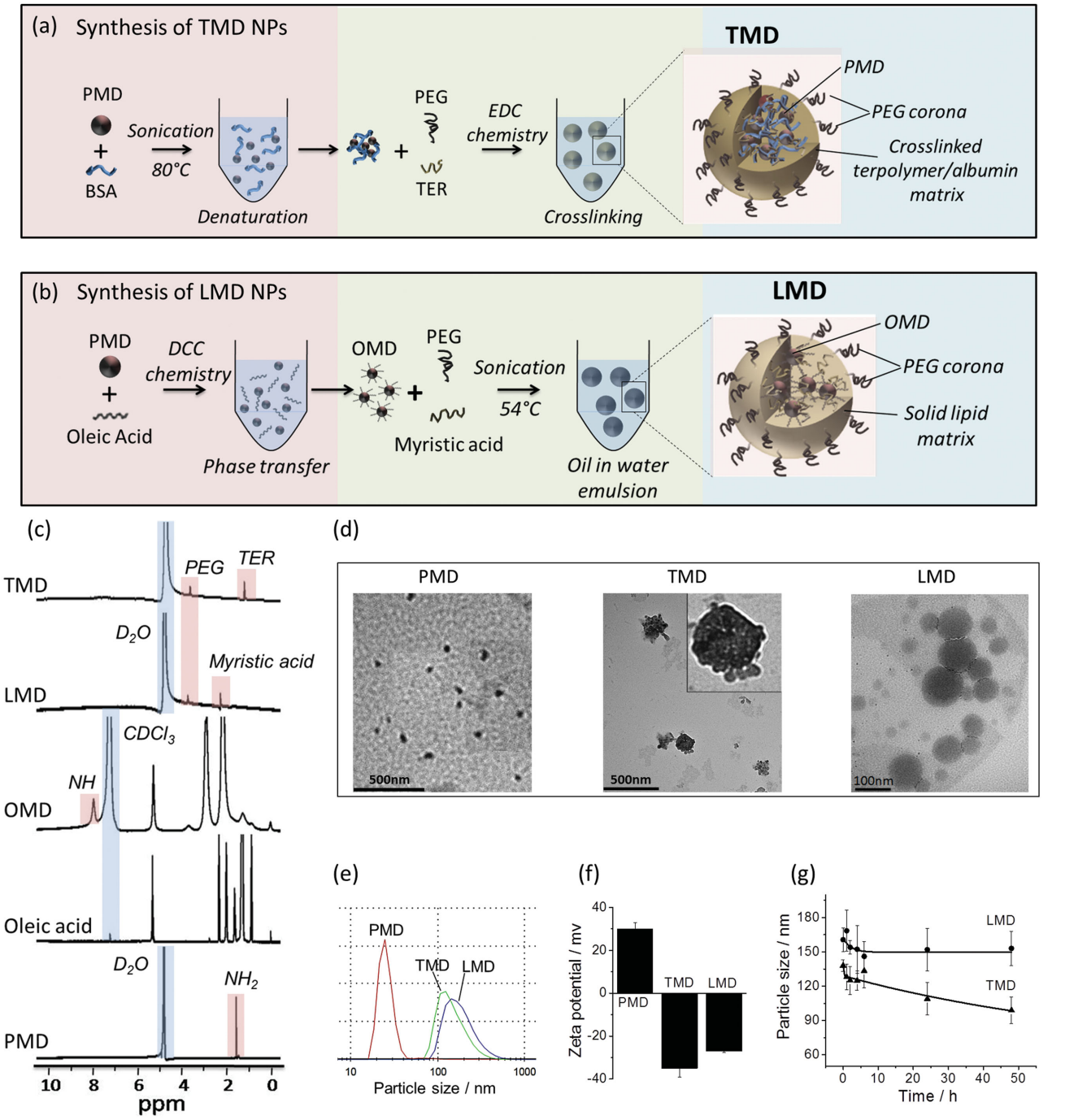

Figure 1. Characterization of oxygen-generating MnO_2 NP hybrids. a) A schematic diagram of TMD and its synthesis. Precursor PMD is loaded in a denatured BSA matrix crosslinked with a graft terpolymer and with a PEG-like brush on the surface. b) A schematic diagram of LMD and its synthesis. PMD is transferred to a hydrophobic phase by covalent conjugation of oleic acid on the NP surfaces (OMD). The hydrophobic particles are then loaded in a solid lipid matrix of Myristic acid with a PEG-like brush on the surface. c) ^{1}H NMR characterization. The spectra show the successful conjugation of oleic acid on the surfaces of PMD precursor NPs and the detection of the PEG chains on the surfaces of the hybrid TMD and LMD particles. d) TEM images of PMD, TMD, and LMD NPs. e) Size distribution (number %) of PMD (≈30 nm), TMD (≈140 nm), and LMD (≈170 nm). f) Zeta potential of the NPs. By loading PMD in TMD or LMD, zeta potential decreased from +30 mV to ≈ −30 mV. g) Colloidal stability of TMD and LMD NPs over time in αMEM cell medium containing 50% FBS at 37 °C.

hydrophobic matrix, PMD was first transferred from aqueous to organic phase by saturating their surfaces with hydrophobic molecules. This was achieved by covalent conjugation of oleic acid to the amine groups of polyelectrolyte (poly(allylamine hydrochloride), PAH) present on the surface of PMD as represented in Figure SI.2a, Supporting Information. The

conjugation was confirmed by recording the absorption spectrum of oleic acid capped PMD NPs (OMD) (Figure SI.2b, Supporting Information). The sharp UV–vis absorption peak of washed OMD NPs at around 270 nm represents the typical absorption of oleic acid. The covalent linkage was also confirmed by nuclear magnetic resonance (NMR) (Figure 1c). The NMR spectrum of OMD NPs showed resonance peaks located in the region 1.0–3.0 ppm referent to oleic acid, together with a new peak at around 8 ppm attributed to the NH group resulted from the reaction of amine groups from PAH and carboxylic acid groups from the oleic acid. Hydrophobic OMD were then loaded in the solid lipid using an oil-in-water emulsion method, by sonicating the mixture of OMD, myristic acid, and lipid-PEG (2 and 5 kDa) at 54 °C (Figure 1b).

The loading capacity of the hybrid TMD and LMD NPs, defined as the total loading of PMD added during NP preparation, was 90%–100%, as confirmed by UV–vis spectroscopy (data not shown). The quantitative analysis was performed using inductively coupled plasma atomic emission spectroscopy (ICP-AES) to accurately determine the metal ion concentration in the hybrid NPs. Functionalization of the surface of the hybrid NPs with PEG was accomplished by adding lipid-PEG during the preparation of the NPs. Through this method, the lipid tail end of the lipid-PEG anchors to the core of the matrix, while its hydrophilic PEG chain extends to the outer surface creating a PEG-like brush on the surface of the NPs. Owing to the fluidity of the PEG chain, it was possible to apply NMR to detect PEG on the surface of the hybrid NPs (Figure 1c). Both TMD and LMD showed a peak around 3.6 ppm characteristic of PEG (Figure SI.3, Supporting Information), confirming the presence of PEG corona on the surface of NPs. NMR characterization also revealed peaks characteristic of the hybrid matrices, as seen in Figure 1c. A peak around 1.5 ppm, characteristic of the TER,[17] was observed in the TMD spectra, whereas a peak around 2.3 ppm, characteristic of the myristic acid, was detected in the LMD NPs. Interestingly, NMR peaks of the loaded PMD or OMD were not detected, suggesting the complete covering of the precursor NPs by the terpolymer/protein or the polymer/lipid matrices.

The size and morphology of the hybrid NPs were observed by transmission electron microscope (TEM). All three NPs (PMD, TMD, and LMD) presented definite size distributions with no apparent aggregates (Figure 1d). PMD NPs appeared to be smaller than 30 nm in size with nearly spherical shape. TMD NPs presented a grape-like morphology with particle size around 140 nm. The hydrophobic LMD NPs were smooth spheres as shown by TEM analysis with an average diameter of 170 nm. In addition, all NPs exhibited dark contrast under TEM attributable to the presence of metal ions in the nanostructures. The size of the NPs was further confirmed by dynamic light scattering (Figure 1e). The values were in good agreement with TEM analysis. Zeta potential measurements revealed a drastic change in the surface charge of the NPs from +30 mV for the PMD to −35 and −27 mV for the TMD and LMD, respectively (Figure 1f). The higher negative surface charge of TMD and LMD correlates to the presence of carboxylic acid groups of terpolymer or myristic acid on the surface of the hybrid NPs, along with hydroxyl head of PEG molecules. In contrast to PMD NPs which showed poor colloidal stability in saline and cell culture media,[9] the higher negative surface charge and hydrophilic polymer chains on the hybrid NPs prevented them from aggregation in these media. TMD and LMD suspensions showed good colloidal stability over time at 37 °C in α-minimum essential media (αMEM) cell medium containing 50% fetal bovine serum (FBS) (Figure 1g) to better represent systemic circulation conditions. No significant change in particle size was observed for LMD NPs over 48 h of incubation; this could be due to the solid structure of lipid matrix and higher melting point of myristic acid (54 °C). However, for TMD NPs a slight decrease in particle size over time was observed, attributable to the soft hydrogel-like texture of these NPs which could interact with serum proteins and change hydration degree.

2.2. Matrix Material and Structure of Hybrid NPs Influence Reaction Kinetics and pH-Dependent Reactivity In Vitro

In a previous study we have demonstrated the reactivity of AMD NPs toward endogenous H_2O_2 and protons for the production of oxygen and increase of pH simultaneously in aqueous solution.[9] This reaction scheme is presented in **Figure 2**a. It is known that the TME is slightly more acidic (≈pH 6.8) than normal tissue and blood (pH 7.4), and the pH becomes even more acidic in the intracellular endosome/lysosome (pH 5.5). Hence we hypothesized that the hybrid NPs could exhibit higher reactivity at lower pH in the TME and in endosomes/lysosomes. To verify this, we studied the pH dependent H_2O_2 consumption and oxygen generation in presence of hybrid NPs of varying hydrophobicity and structures. These results could provide some insights into the differential reactivity of the NPs in the blood circulation, the TME, and intracellular compartments.

The pH dependent reactivity of the NPs in solution was evaluated by measuring the residual concentration of H_2O_2 over time using a PeroXOquant assay kit. Figure 2b shows the percentage of H_2O_2 (500×10^{-6} M) quenched upon reaction with 100×10^{-6} M MnO_2 of PMD, TMD, or LMD NPs at three different pH values (normal tissue pH 7.4, tumor pH 6.8, and endosomal/lysosomal pH 5.5). For all pH values tested, the reactivity of the NPs was in an order PMD >> TMD > LMD. The PMD NPs were able to quench 100% of the H_2O_2 in less than 10 min at all three pH values. This fast reactivity was not surprising since there was no barrier between the PMD NPs and reactants (H_2O_2 and H^+) allowing the reaction to occur almost instantly. As expected, the hydrophobic solid matrix in the LMD NPs slowed down the diffusion of reactants and products, leading to a lower H_2O_2 quenching rate.

For all three NP formulations a gradual increase in reactivity was observed as the pH of the medium decreased from pH 7.4 to pH 5.5 Although the reaction rate for PMD at different pH values was difficult to evaluate, a slightly higher reaction rate at pH 5.5 than at pH 7.4 at the initial time points (inset Figure 2b (PMD)) was detected. On the other hand, strong dependence of reactivity toward H_2O_2 was clearly seen for TMD and LMD. The initial rates of H_2O_2 quenching (R_0) were calculated from the slope of the first linear portion of the plots and summarized in **Table 1**. After 1 h incubation at 37 °C, TMD NPs were

(a)

1) $2MnO_2 + H_2O_2 \rightarrow 2MnOOH + O_2$

2) $2MnOOH + 4H^+ + H_2O_2 \rightarrow 2Mn^{2+} + 4H_2O + O_2$ *(non catalytic)*

3) $2MnOOH + 2H^+ \rightarrow MnO_2 + Mn^{2+} + 2H_2O$ *(catalytic)*

4) $MnO_2 + H_2O_2 + 2H^+ \rightarrow O_2 + Mn^{2+} + 2H_2O$

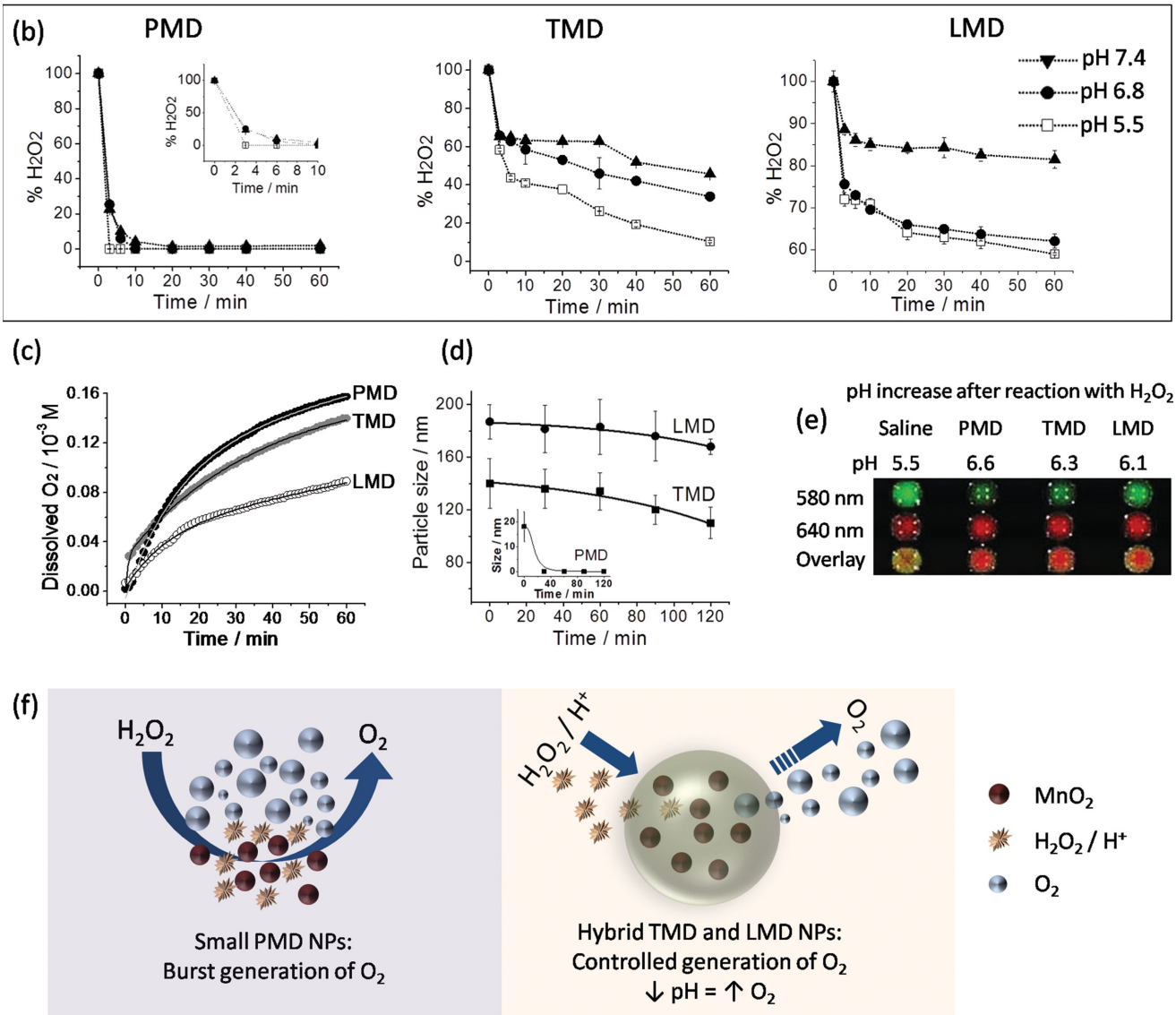

Figure 2. a) A reaction scheme showing the reactivity of MnO_2 toward H_2O_2 for the production of O_2 and removal of protons. The reaction is not purely catalytic and the breakdown of MnO_2 to Mn^{2+} is favored at more acidic pH. b) Panel comparing the in vitro reactivity of PMD, TMD, and LMD NPs toward endogenous H_2O_2 at normal tissue pH 7.4 to acidic tumor pH 6.8 and endosomal/lysosomal pH 5.5. c) O_2 generation by addition of H_2O_2 to different NPs suspensions. d) NP size change during reaction with H_2O_2. Error bars are SEM for $n = 3$ independent experiments. e) Effects of NPs on pH increase after reaction with H_2O_2 using pH-sensitive fluorescent dye (SNARF-4F). All experiments were performed ($n = 3$) in normal saline at 37 °C and at endogenous H_2O_2 level (500×10^{-6} M) and same NP concentration (100×10^{-6} M). f) A schematic representation of the different reactivity of the NPs toward H_2O_2. Free PMD reacts almost instantly with H_2O_2 leading to a burst generation of O_2 independent of the pH. In contrast, hybrid TMD and LMD NPs show prolonged O_2 release and increased reactivity toward endogenous H_2O_2 at acidic pH. The pH-dependent reactivity renders the hybrid NPs higher H_2O_2 quenching activity in acidic TME than in the systemic circulation and normal tissue with higher pH.

Table 1. Effect of pH on the rate of H_2O_2 quenching of the NPs (PMD, TMD and LMD)* in normal saline at 37 °C. The initial rate (R_0) was calculated from the slope of the first linear portion of the curves from Figure 2b, and the relative amount of H_2O_2 was calculated using the percent of remaining H_2O_2 in the solution after 1 h. (n = 3)

	Rate of H_2O_2 quenching (R_0) 10^{-6} M H_2O_2/10^{-6} M MnO_2/min			Relative amount of H_2O_2 quenched after 1 h at different pH (from pH 7.4 to 6.8 and to 5.5)		
	pH 7.4	pH 6.8	pH 5.5	pH 6.8/pH 7.4	pH 5.5/pH 6.8	pH 5.5/pH 7.4
PMD[a)]	0.75 ± 0.3	0.8 ± 0.2	1.65 ± 0.05	1.0	1.0	1.0
TMD[b)]	0.29 ± 0.1	0.31 ± 0.1	0.47 ± 0.1	1.21	1.34	1.64
LMD[c)]	0.12 ± 0.04	0.22 ± 0.1	0.23 ± 0.1	2.0	1.07	2.16

[a)]PMD: polyeletrolyte-coated MnO_2 NPs (precursor, burst O_2 release); [b)]TMD: MnO_2 embedded in a hydrophilic terpolymer/protein matrix (fast acting O_2 release); [c)]LMD: MnO_2 embedded in a hydrophobic polymer/solid lipid matrix (slow acting O_2 release).

able to quench 50%, 60%, and 85% of the H_2O_2 while LMD NPs quenched 15%, 38%, and 40% of the H_2O_2 at pH 7.4, 6.8, and 5.5, respectively. The relative increase in H_2O_2 quenching as pH decreased from 7.4 to 6.8 and to 5.5 was 1.21, 1.34, and 1.64 for TMD and 2.0, 1.07, and 2.16 for LMD NPs, respectively.

The higher reactivity of NPs at lower pH could be attributed to the higher concentration of H^+ ions in the medium, which increases the reaction rate with H_2O_2 and MnO_2 (Figure 2a).[9] We further compared the reactivity of the NPs by measuring generated O_2 levels in solution at 37 °C containing 100×10^{-6} M of MnO_2 in the NPs and 500×10^{-6} M of H_2O_2. The reaction was performed in normal saline (pH 5.5) inside an in-house-made semi-sealed hypoxia-maintaining chamber, and dissolved O_2 was monitored over time for 1 h with a commercially available oxygen probe. Consistent with the H_2O_2 quenching results, PMD NPs showed the fastest O_2 generation rate, with 0.15×10^{-3} MO_2 produced in 1 h, followed by TMD NPs (0.14×10^{-3} M), and LMD NPs (0.08×10^{-3} M). Although a quantitative correlation between the rates of H_2O_2 quenching (Figure 2b) and the rates of generated O_2 (Figure 2c) was not attempted due to uncontrollable variables (i.e., pH of the solution, which increased slightly during reaction and use of a semi-sealed system), the same trend in the reactivity of the NPs (PMD > TMD > LMD) was observed in both experiments.

Change in NPs size upon reaction with H_2O_2 was also studied (Figure 2d). We found that PMD NPs were completely consumed within first 40 min of reaction (Figure 2d inset), confirming the fast reactivity of free PMD. In contrast, the hybrid NPs showed a good sustainability in particle size during the reaction. A more dramatic decrease in NP size was observed for the TMD than the LMD NPs, probably due to a partial consumption of the MnO_2 load which can leave the softer terpolymer/protein matrix mechanically less stable than the solid lipid matrix of the LMD.

Last, we verified the changes in microenvironmental pH caused by the action of the NPs (Figure 2e). The reaction between MnO_2 and H_2O_2 is known to increase the local pH due to the consumption of protons and the formation of alkaline intermediates (Figure 2a).[9] Here, we utilized multispectral pH sensitive dye (SNARF-4F) to verify whether the reaction between the hybrid NPs and H_2O_2 would also cause changes in pH. SNARF-4F was selected for in vitro pH imaging (pKa ≈ 6.4) since it is sensitive to pH values close to that of the TME (pH ≈ 6.8). Moreover it allowed the observation of small pH changes in a small volume comparable to the tumor volume (i.e., 200 µL). The experiment was performed in a 96 well plate under the same conditions described above (100×10^{-6} M of MnO_2 and 500×10^{-6} M of H_2O_2 in normal saline pH 5.5 at 37 °C for 1 h). These results are summarized in Figure 2e. Compared to saline control, a significant increase of the pH in the microplate wells was observed for all three NPs. After 1 h, the pH increased from 5.5 in the saline control to 6.6, 6.3, and 6.1 for PMD, TMD, and LMD NPs, respectively. These results are consistent with the differential reactivity observed for the NPs in the order PDM > TMD > LMD.

In summary, the results shown in Figure 2a–e revealed the impact of material property and structure of the NPs on the reactivity of the MnO_2. The hydrophilic, grape cluster-shaped TMD showed slower reactivity compared to PMD but faster when compared to hydrophobic LMD NPs. These results suggest that the terpolymer/protein or polymer/lipid matrices of the hybrid NPs create a diffusion barrier and differential reaction sites that can tune the reactivity of MnO_2 payload. The hydrophobic nature of LMD NPs further limits the inward diffusion of H_2O_2 and protons, resulting in slower reactivity compared to hydrophilic terpolymer/protein matrix of TMD NPs where diffusion is expected to be more efficient. The different reactivity of the NPs is illustrated schematically in Figure 2f. Overall, the reactivity of the hybrid NPs increases significantly as the pH is reduced from normal tissue pH 7.4 to acidic tumor pH 6.8 and endosomal/lysosomal pH 5.5. This effect is even more pronounced for the LMD NPs. The pH-dependent reactivity rendered the LMD a higher H_2O_2 quenching activity in acidic tumor microenvironment than in the systemic circulation and normal tissue with higher pH. Thus, we speculated that LMD NPs could be a better candidate for systemic administration of the NPs than the TMD. This hypothesis was examined through the following experiments.

2.3. Hybrid NPs Show Controlled Oxygen Generation in Whole Blood

Photoacoustic (PA) imaging measures oxygen saturation (sO_2) in the blood by the differential optical absorption of oxygenated and deoxygenated hemoglobin at different wavelengths. This can be directly correlated with changes in O_2 concentration in the blood.[20] In a previous study we have demonstrated the effect of AMD NPs on the oxygen saturation in the tumor in vivo and found that IT injection with AMD increased tumor oxygenation by 45% within minutes.[9] Since PA measures oxygen saturation in the blood, we speculated that the O_2 generated

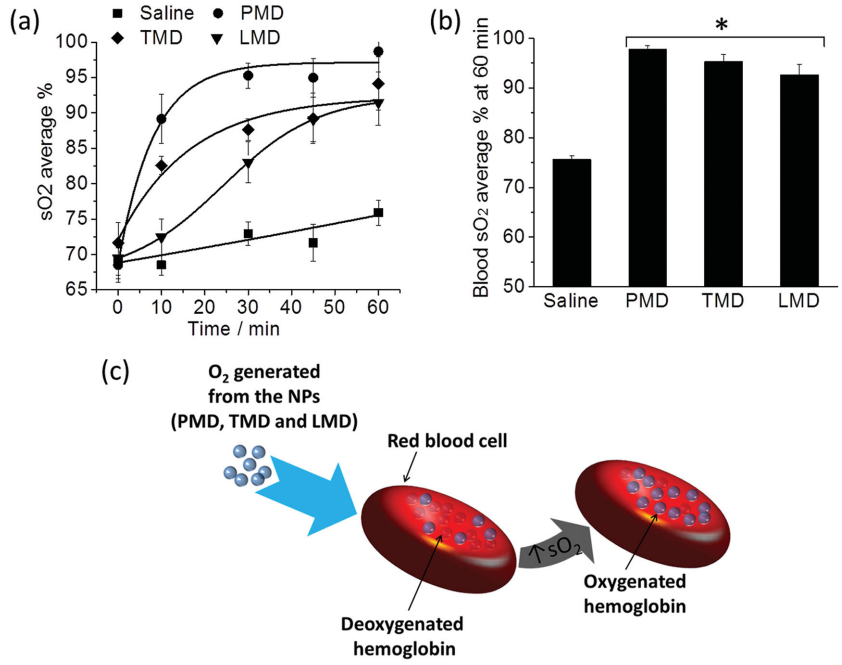

Figure 3. In vitro oxygen saturation (sO_2) in whole blood. a) Increase of sO_2 in blood over time following incubation with NPs (PMD, TMD, and LMD, 100×10^{-6} M) and H_2O_2 (500×10^{-6} M) at 37 °C. Saline was used as a control. b) Comparison of average blood sO_2 after 1 h incubation. 2D PA images of tube phantoms containing blood and treatments ($n = 3$/group) were used to determine an increase in sO_2 average %. (*) Statistically significant increase (*$p < 0.01$) in sO_2 as compared to saline (control). c) Schematic representation showing the increase in sO_2 in blood due to the action of the NPs. O_2, generated by the reaction of the PMD, TMD, or LMD NPs with H_2O_2, binds to deoxygenated hemoglobin in red blood cells leading to oxygenated hemoglobin, thus an increase in the PA signal is detected.

by the action of the AMD toward endogenous H_2O_2 produced by the cancer cells quickly diffused through the tumor mass, penetrated the tumor vasculature, and bound to deoxygenated hemoglobin in the red blood cells, thus generating an increase in the PA signal.

Here we wanted to verify the O_2 generating properties of the new hybrid NPs TMD and LMD directly in the blood and compare the effect of NP materials and structure on the kinetics of oxygen saturation in this system (**Figure 3**). A tube phantom with the PA imaging system was used to measure sO_2 average in whole rat blood over time upon incubation with TMD, LMD, or PMD (100×10^{-6} M) with saline as control. In vivo, H_2O_2 is constantly generated in the body at endogenous levels (100×10^{-6} M up to 1×10^{-3} M in tissue and body fluids).[21] Since our experiments were performed in vitro, exogenous H_2O_2 was added at a physiological concentration (500×10^{-6} M) to ensure similar conditions to all groups. Similar to the O_2 generation in saline (Figure 2c), the three NPs showed distinct rates of O_2 production in the blood (Figure 3a). Small PMD showed a burst O_2 generation reaching 90% of oxygen saturation within 10 min. In contrast, the hybrid TMD and LMD NPs showed a more controlled and prolonged generation of O_2 in the blood with maximum oxygen saturation (90–95%) being reached within 60 min. The slowest sO_2 rate was obtained with the hydrophobic LMD. Despite the different kinetics, all NPs reached the maximum oxygen saturation within 60 min (Figure 3b) showing that the different NP structures can modulate the rates of O_2 generation likely through the diffusion of H_2O_2 and O_2 in and out of the terpolymer/protein or polymer/lipid matrices, respectively, without compromising the reactivity of the MnO_2 in whole blood. These results also demonstrated that the hybrid MnO_2 NPs can react with physiological H_2O_2 levels in the blood and generate O_2 that will bind to hemoglobin and have the potential to reach organs or tissue deficient in O_2 (such as the hypoxic tumor). More importantly, these results showed that the hybrid NPs, particularly the LMD, promoted significantly slower O_2 generation rates in the blood compared to free PMD. This is highly desirable for prolonged circulation of the NPs prior to accumulation in a tumor via the EPR effect without burst O_2 release in the vasculature during circulation.

2.4. Uptake of Hybrid NPs by Murine and Human Breast Cancer Cells

It is known that cancer cells can respond to low tumor oxygenation by adapting their glucose metabolism and mitochondrial respiration mediated by HIFs and this mechanism confers a survival and growth advantage to hypoxic tumor cells.[2] Therefore, direct interaction of the NPs with cancer cells may play an important role in the modulation of the TME including HIF-1α regulation. Here, we used two different cell lines, murine EMT6 and human MDA-MB-231 breast cancer cells to study the cellular uptake of TMD and LMD NPs and cell viability. For uptake studies, fluorescent NPs were prepared by covalently grafting fluoresceinamine to BSA or myristic acid prior to the TMD and LMD NP preparation, respectively. A strong fluorescent signal confirmed the successful labelling of the hybrid NPs. Also, there was no significant change in the particle size and surface charge of the fluorescent NPs (data not shown), suggesting it is reasonable to assume that the labeled particles would interact with cells similarly to the unlabeled particles.

The cells were incubated with fluorescent NPs (100×10^{-6} M) for 1 h at 37 °C, and cell uptake was visualized using confocal laser scanning microscopy. The cell nuclei were stained blue to differentiate cellular compartments. The images revealed intensive accumulation and uniform distribution of TMD and LMD NPs in the cytoplasm and around the nuclei of the cells, depicting internalization and accumulation of TMD and LMD NPs by EMT6 and MDA-MB-231 breast cancer cells within 1 h incubation period (**Figure 4**a,b). The effective cellular uptake of TMD and LMD NPs observed here is consistent with previous findings that NPs made with terpolymer[17] or solid lipid are taken up by cancer cells by endocytosis.[19,22] Cancer cell viability was also investigated using a standard methyl thiazol

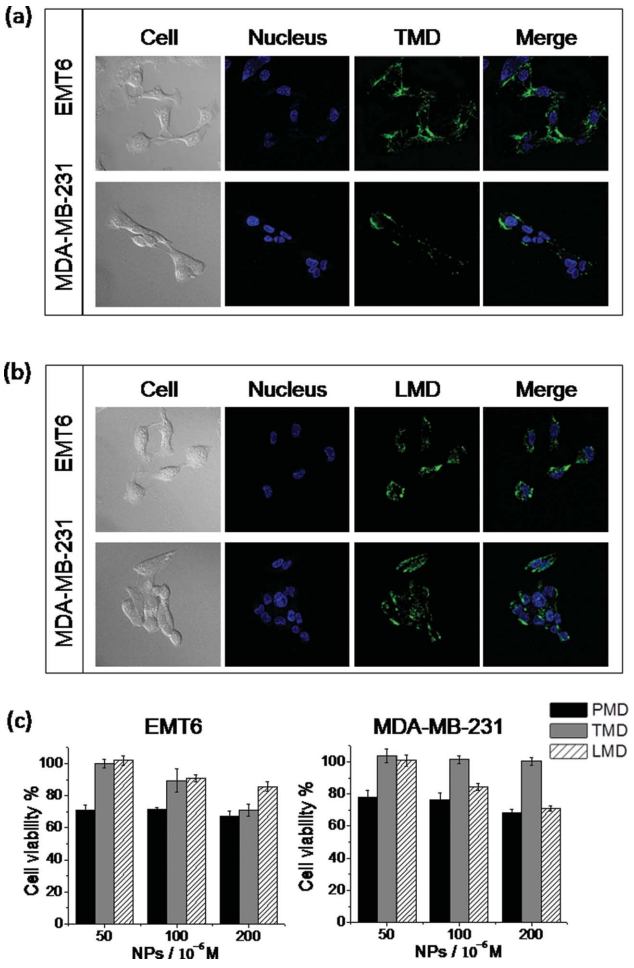

Figure 4. Fluorescence images of cellular uptake of hybrid NPs at 37 °C by murine EMT6 and human MDA-MB-231 breast cancer cells following 1 h incubation with a) TMD and b) LMD NPs. c) Viability of murine EMT6 and human MDA-MB-231 cells (10^5 cells mL^{-1}) exposed to various concentrations of PMD, TMD, and LMD NPs for 48 h. Percentage of cell viability was determined with MTT assay and is presented as relative to the control.

tetrazolium (MTT) assay after incubation with different concentrations (50×10^{-6}, 100×10^{-6}, and 200×10^{-6} M) of PMD, TMD, and LMD NPs for 48 h. As shown in Figure 4c, while PMD NPs caused noticeable toxicity, the hybrid NPs were considered nontoxic with cell viability >80% with the NP concentrations of up to 100×10^{-6} M.

2.5. Hybrid NPs are Safe for Systemic Delivery

Despite the large number of NP systems investigated for cancer therapy, the safety of many hybrid materials still remains a concern for their translation to clinic.[23] In general, NP systems tend to accumulate in the liver due to rapid clearance by the mononuclear phagocytic system when injected IV.[23,24] Although toxicity of MnO_2 NPs to the liver and kidney by long-term oral exposure has been investigated at doses up to 1000 mg kg^{-1} body weight (bw)[25], no study has been reported for IV administered PMD and hybrid MnO_2 NPs. Thus we assessed the safety and dose tolerance of the hybrid NPs using liver cells (hepatocytes) in vitro, as well as their effect on healthy tissue in vivo after chronic exposure to NPs through IV administration (**Figure 5**). Note that the MnO_2 doses required for in vivo oxygen generation are much lower (<1 mg kg^{-1} bw)[9] than what was used in a previous oral investigation.[25]

For in vitro studies we applied a standard method for drug development using freshly isolated hepatocytes from rat liver. This method assumes that a high dose/short time exposure in vitro simulates a low dose/long time exposure in vivo of the tested substance.[26] Hepatocytes were incubated for 2 h with NPs at two different concentrations: the optimal concentration required for oxygen generation at physiological conditions (100×10^{-6} M), and four times this concentration (400×10^{-6} M) to simulate a high particle exposure. We found that overall, the hybrid NPs did not cause noticeable loss of hepatocyte viability (Figure 5a) or damage to the mitochondrial membrane via loss of membrane potential (Figure 5b) at both concentrations. However a moderate decrease in cell viability and mitochondrial membrane potential (MMP) was observed for free PMD NPs at 400×10^{-6} M as compared to controls (≈74% and 85%, respectively). In contrast, the hybrid NPs generated much less ROS than PMD in the order TMD ≈ LMD << PMD (Figure 5c). The ROS production increased more than 2-fold as MnO_2 concentration was increased from 100×10^{-6} M to 400×10^{-6} M. It is known that nanomaterials of other metal oxides, including MnO_2 nanowires, can induce ROS formation and MMP reduction in cells by various mechanisms not completely understood which are also correlated to differences in surface charge and particle size.[27] Our results show that NP-induced intracellular ROS formation can be drastically reduced by loading PMD in the hybrid matrices. Although the in vitro result showed higher ROS production in the hepatocytes from all NPs studied as compared to saline control, the NP concentrations applied to the hepatocytes were much higher than the actual NP concentration the liver would receive in the in vivo studies, due to distribution of the NPs in the blood, deposition in other tissues, and elimination from the circulation.

To investigate the in vivo safety of the hybrid NPs, mice were treated IV with a suspension of PMD, TMD, or LMD in sterile saline at a dose of 0.7 mg kg^{-1} bw (200 µL of 1×10^{-3} M MnO_2 per mouse). Minutes post IV injection, mice treated with PMD showed increased heart rates and a difficulty in breathing, probably due to the small size and highly positive charge of these NPs and their fast reactivity in the systemic circulation (which can lead to electrolyte imbalance and blood cell toxicity). For these reasons the treatment was discontinued for this group. In contrast, animals treated with hybrid TMD or LMD NPs did not show any sign of acute toxicity (Figure 5d). TMD and LMD-treated groups continued receiving daily IV injections with hybrid NPs for 7 consecutive days with no external sign of toxicity or adverse symptoms (including weight loss or change in food intake) being noticed during the treatment period (data not shown). At the end of the experiment, animals were sacrificed and selected organs (lungs, heart, kidneys, spleen, and liver) were resected, formalin fixed, and stained with haematoxylin and eosin (H&E) for histopathology analysis (Figure 5e). There was no histological evidence of accumulated toxicity in

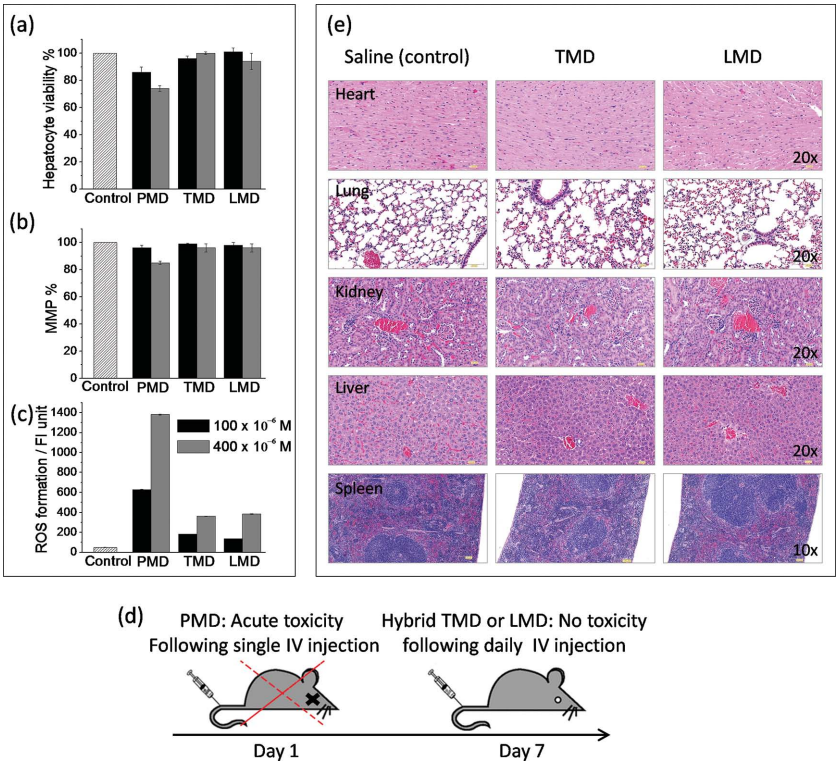

Figure 5. In vitro and in vivo safety of NPs. Left Panel: Effect of NPs (PMD, TMD, and LMD) on a) hepatocyte viability, b) MMP, and c) ROS formation. Hepatocytes isolated from rat liver were incubated with two different NP concentrations, 100×10^{-6} M (grey bars) and 400×10^{-6} M (black bars) for 2 h . FI, fluorescence intensity. d) Schematic representation showing the effect of the different NPs on mice. Free PMD NPs showed severe acute toxicity following IV injection in mice. In contrast, hybrid NPs TMD and LMD were well tolerated by mice following daily IV treatment for a week. e) Effect of NPs on healthy tissue. Panel: Representative H&E-stained tissue sections of various organs after daily systemic treatment with TMD and LMD NPs. NPs were administered IV (200 µL, 1×10^{-3} M) for 7 consecutive days. Saline was used as a control ($n = 3$/group).

the analyzed organs associated with IV administration of TMD or LMD NPs daily for 7 days, as compared to saline controls. These results demonstrated the excellent in vivo biocompatibility of the hybrid NPs and the importance of the hybrid system in mitigating toxicity caused by free PMD via systemic administration.

2.6. Matrix Material and Structure of Hybrid NPs Influence Their Accumulation and Retention in the Tumor

To demonstrate the effectiveness of the hybrid NPs for potential treatment of solid tumors in vivo, whole body fluorescence imaging was performed to study the tumor accumulation and biodistribution of the TMD and LMD NPs after their systemic administration. For in vivo fluorescence imaging, near-infrared labeled NPs were obtained by adding indocyanine green (ICG) during the preparation of NPs. A strong fluorescence signal from washed NPs confirmed the successful loading of the near-infra red dye into terpolymer/protein and polymer/lipid matrices. ICG was selected for in vivo imaging due to its longer emission wavelength (≈800 nm), which enables deep tissue penetration and lowers interference with tissue auto-fluorescence. These properties of ICG made it possible to set the detection limit to completely exclude the background signal of tissue auto-fluorescence.

For in vivo whole body imaging, 200 µL of near-infrared labelled TMD or LMD NPs (1×10^{-3} M in saline) was injected IV in the tail vein of EMT6 tumor bearing mice, and animals were imaged at different time intervals up to 24 h (0, 30, 1, 2, 4, and 24 h) (**Figure 6**). Following IV injections, a large increase in fluorescence signal was observed all over the body of the mouse for both TMD and LMD, with accumulation in the liver and spleen after 30 min. For TMD, higher NP fluorescence intensity was retained in the abdominal region (i.e., liver, spleen, and kidneys) after 24 h, and relatively weak fluorescence intensity was detected in the tumor tissue (Figure 6a). On the other hand, together with liver uptake, LMD NPs also displayed substantial accumulation in the tumor tissue only 1 h after IV injection, and tumor fluorescence signal persisted up to 24 h indicating the higher tumor retention of LMD NPs compared to TMD NPs (Figure 6b). For both types of NPs the whole body fluorescence intensity was maintained even after 24 h, confirming the long circulation time of hybrid NPs, probably due to the PEG moieties present on the surface of the NPs. The surface modification of NPs with PEG has previously been shown improve blood circulation lifetime after systemic administration.[28]

Additionally, ex vivo images of organs (liver, tumor, lungs, heart, spleen, and intestines) excised from mice sacrificed at 4 and 24 h post injection also confirmed the higher liver uptake for TMD and LMD NPs at 4 h post injection (Figure 6a,b). A decrease in liver fluorescence was observed after 24 h, which was more significant for LMD NPs. Furthermore, the LMD NPs exhibited relatively higher tumor uptake at 4 h compare to other organs except liver, and the tumor fluorescence was maintained even at 24 h confirming the high retention of these NPs. Consistent with in vivo whole body imaging, ex vivo imaging showed lower tumor uptake for TMD NPs at 4 h, while no NP fluorescence was observed at 24 h suggesting faster clearance of these NPs from tumor tissue. For both NPs, a strong fluorescence signal was detected in kidneys at 4 h post injection which dramatically decreased after 24 h, suggesting clearance of the NPs through the renal route.

For both TMD and LMD, passive tumor accumulation of the NPs was expected to occur through the EPR effect, attributed to the leaky nature of immature vessels in the tumor.[17,19] Despite comparable size range, charge, and surface chemistry (i.e., PEG), the in vivo and ex vivo near-infrared fluorescence images demonstrated a better accumulation and extended tumor retention of the LMD compared to the TMD NPs. The lower tumor

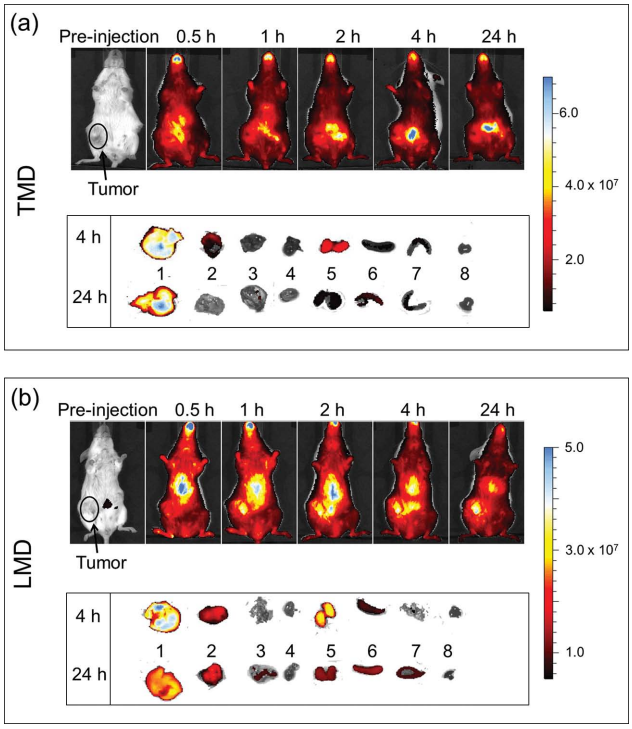

Figure 6. Biodistribution and tumor accumulation of a) TMD and b) LMD NPs. Top panels: Representative optical images of EMT6 tumor-bearing mice with IV injected near-infrared-labeled NPs at various times up to 24 h. Bottom panels: Representative ex vivo images showing the accumulation of the NPs in various organs at 4 and 24 h post-IV injections. The numbers (1–8) correspond to the different organs: 1) liver, 2) tumor, 3) lungs, 4) heart, 5) kidneys, 6) spleen, 7) intestines, and 8) blood.

accumulation of TMD NPs might be due to the fast action of the TMD NPs toward H_2O_2 (and consequent consumption of the loaded MnO_2) which may cause these NPs to breakdown faster in the systemic circulation and tumor, thus decreasing their accumulation and retention in the tumor. The different tumor accumulation and retention profiles and oxygen generation rates of the TMD and LMD NPs should directly reflect their abilities to promote tumor oxygenation and decrease of tumor hypoxia. These findings are discussed in detail in the following section.

2.7. Effect of Material Hydrophobicity and Structure of Hybrid NPs on Tumor Oxygenation

We next wanted to know how the material hydrophobicity and structure of the hybrid NPs affected tumor hypoxia and HIF-1α levels. We also wanted to compare the effect of the NPs via local IT injection and systemic IV administration to determine the optimal delivery route and timing for tumor oxygenation following treatment with the NPs. To this end, we applied immunofluorescence (IF), a method utilized for identification and quantification of metabolic markers in tumors,[29] to investigate the effect of the IT and IV treatments with TMD or LMD NPs on hypoxia and HIF-1α in EMT6 murine breast cancer xenografts in mice. This cell line has been extensively used for hypoxia studies both in vitro and in vivo[30] and has been demonstrated to be a good model for evaluation of changes in tumor oxygenation by MnO_2 in vivo.[9]

For visualization of the TME, we utilized fluorescein isothiocyanate (FITC)-pimonidazole and Alexa 594 conjugated antibody for the detection of tumor hypoxia and HIF-1α, respectively. This method provided clear identification of the markers in the whole tumor, as shown in the fluorescence images. Mice treated IT or IV with TMD or LMD NPs were left for various times up to 4 h (0.5, 1, 2, and 4 h) (**Figure 7**) and then the tumors were removed and sectioned for various staining procedures. H&E stain was used for morphological analysis of the tumor and identification of viable tumor areas. As shown in the panels (**Figures 8** and **9**), necrotic tumor areas (mostly composed of dead cells) which are pink in the H&E images appear black in the fluorescence images due to the specific binding of the antibodies to the viable cells. The viable tumor area was also clearly visualized in the blue channel through nuclear staining with 4′,6-diamidino-2-phenylindole (DAPI).

Clear changes in hypoxia and HIF-1α were observed after treatment with the hybrid NPs. Control tumors (Figure 8a) were found to be very hypoxic (90% positive area), showing positive pimonidazole staining throughout the entire viable tumor area. A stronger hypoxic ring, characterized by higher fluorescence intensity, was observed in the areas surrounding the necrotic core. High expression of HIF-1α (70% positive area) was also observed for the control group. No significant differences in hypoxia and HIF-1α were observed between controls treated with saline through IT or IV injection.

Following treatment with IT injection with TMD or LMD NPs, a clear decrease in tumor hypoxia and HIF-1α was visualized with the fluorescence images (Figure 8a). Quantification of the markers was performed for tumors treated with IT injection with TMD or LMD for 0.5, 1, 2, and 4 h and compared to saline controls. In contrast to traditional brown and blue immunohistochemistry (IHC) staining, where the quantification of markers is limited to selected small areas,[31] IF images allowed us to perform quantification of the entire viable tumor area from classified images. We found that hydrophilic TMD NPs showed the fastest tumor oxygenation in vivo. In just 0.5 h post IT injection tumor hypoxia decreased by approximately 70% compared to the saline control group. We attribute this to the fast action of the TMD NPs for the generation of O_2. The effect of the TMD NPs was sustained for 1 h and tumor hypoxia started increasing gradually after 2 and 4 h, possibly due to a faster consumption of the MnO_2 content of hydrophilic NPs upon reaction with endogenous H_2O_2 in the tumor. A slower but more prolonged effect was observed for the hydrophobic LMD NPs. For the LMD group, hypoxia decreased by 33% 0.5 h post IT injection, and was maintained 50% lower than the saline control group for up to 2 h. This prolonged effect was attributed to the more controlled reactivity and slower action of these NPs. For both hybrid NPs, however, tumor hypoxia was still 30% lower than the control 4 h post-treatment.

The decrease in tumor hypoxia by the action of the hybrid NPs was also reflected in a decreased expression of HIF-1α (Figure 8b). Since HIF-1α is a downstream marker of hypoxia, we quantified this marker at the later time points, 2 and 4 h post IT treatment. Interestingly, despite their different effect on

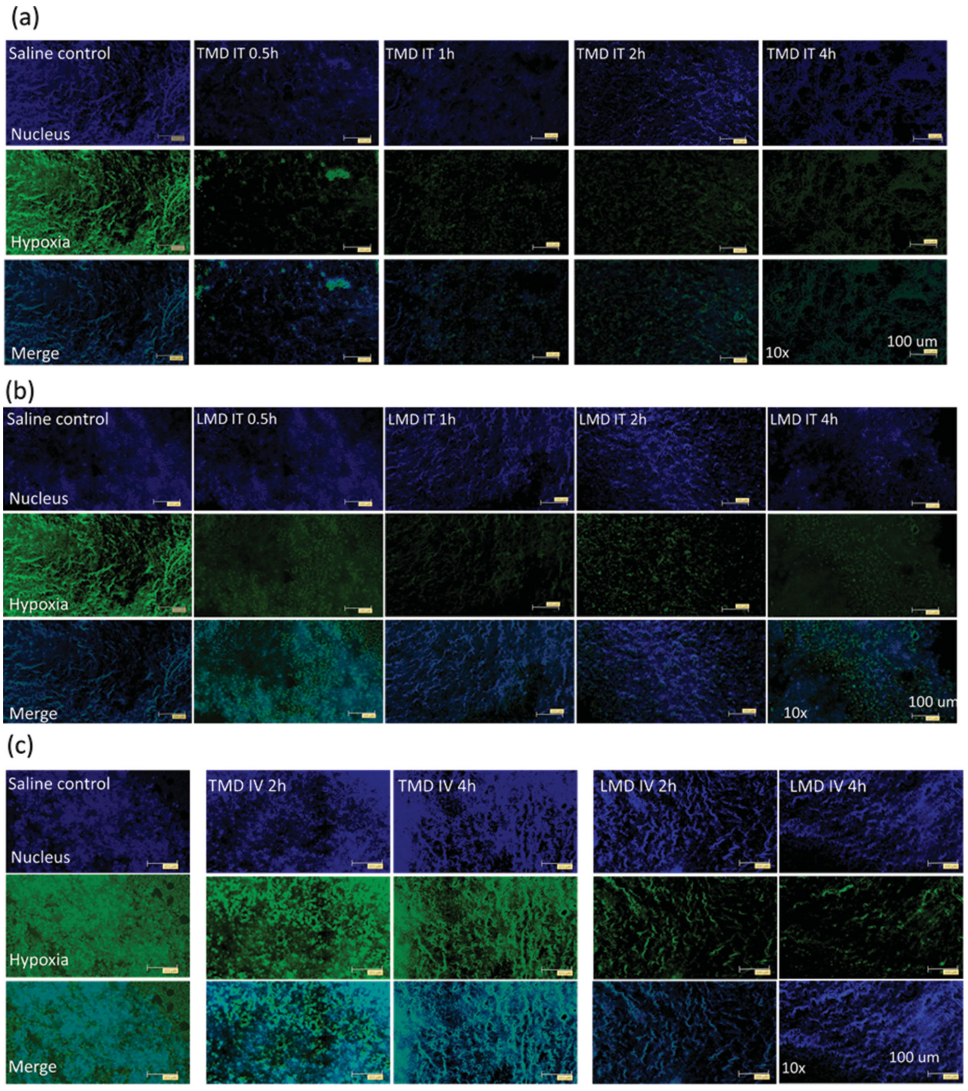

Figure 7. Immunofluorescence detection of tumor hypoxia. Panel shows representative IF images of tumors treated with TMD and LMD NPs through a,b) local IT injection or c) systemic IV injection at various time points up to 4 h. Detection of tumor hypoxia was determined by pimonidazole binding (green) using Hypoxyprobe-1 plus kit. Nuclei (blue) were stained with DAPI.

tumor hypoxia, TMD and LMD NPs led to similar decreases in HIF-1α, of around 40% and 60% after 2 and 4 h, respectively, as compared to saline controls.

For systemic administration, hypoxia and HIF-1α were determined 2 and 4 h post IV injections to allow enough time for the NPs to accumulate in the tumor, as determined by the biodistribution studies previously discussed (Figure 6). Compared to IT treatment, the IV groups had different trends in hypoxia and HIF-1α levels (Figures 7c and 9). Mice treated with IV injections of TMD did not show significant changes in tumor hypoxia or HIF-1α compared to saline controls, probably due to the lower tumor accumulation of TMD NPs. In contrast, the group treated with LMD showed a significant decrease in tumor hypoxia by 30% and 45%, 2 and 4 h post IV injection, respectively. Moreover, at 4 h HIF-1α was decreased by 55%, as compared to saline controls. These results could be attributed to the high tumor accumulation and controlled reactivity of the LMD NPs, which allowed for slower oxygen generation (and probably lower consumption of the MnO_2 payload) in the systemic circulation, good tumor accumulation within 1 h post IV injection, and higher reactivity in the acidic TME.

3. Conclusions

Hybrid NPs were successfully prepared by incorporating small MnO_2-polyelectrolyte-coated (PMD) particles in terpolymer/protein (TMD) or polymer/lipid matrices (LMD) resulting in NPs of different hydrophobicity and structures. The hybrid NPs exhibited significantly improved colloidal properties and biocompatibility in vitro and in vivo as compared to free PMD NPs, with no tissue toxicity found after daily IV administration

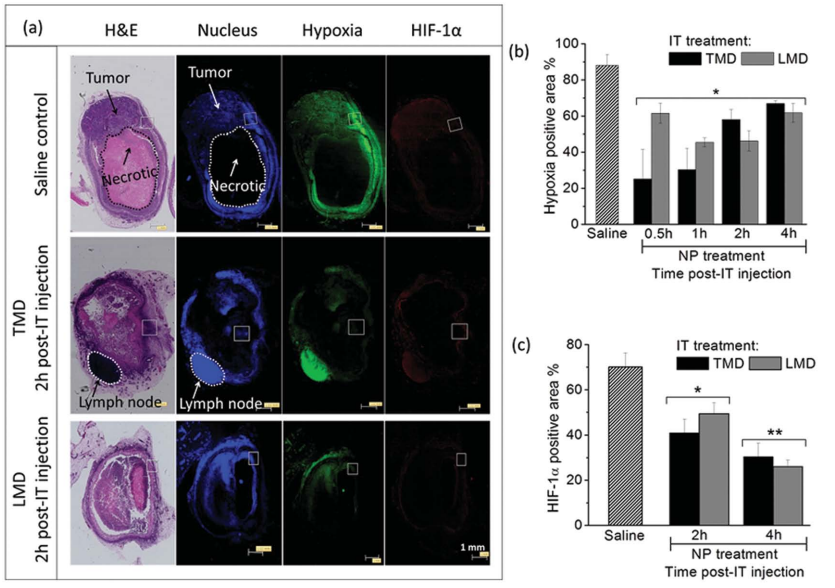

Figure 8. Effect of local IT treatment with hybrid TMD and LMD NPs on tumor hypoxia and HIF-1α. a) Panel showing representative IF images in continuous sections from EMT6 tumors from mice treated with IT injection with the NPs or saline (control) for 2 h. Tumor hypoxia was determined by pimonidazole binding and HIF-1α antibody. Different stains are from continuous sections of a same tumor: H&E, nucleus (blue), pimonidazole (green), HIF-1α (red). Necrotic tumor areas appear in pink in the H&E stain and in black in the fluorescence images. The square insets show a representative viable tumor area. Scale bars correspond to 1 mm. Quantification of b) tumor hypoxia and c) HIF-1α after treatments for up to 4 h, determined from classified images (not shown). (n = 3/group). (*) Statistically significant (*p < 0.01, **p < 0.05) as compared to saline (control) treated groups.

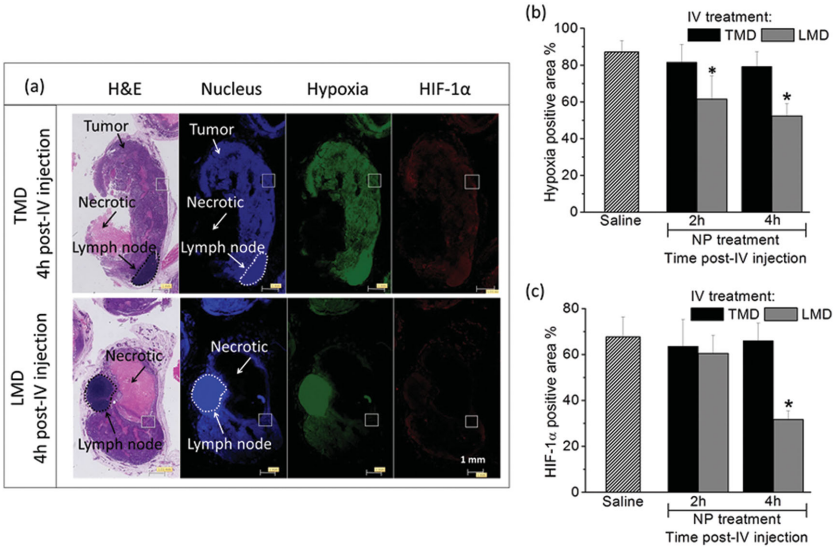

Figure 9. Effect of systemic IV treatment with hybrid TMD and LMD NPs on tumor hypoxia and HIF-1α. a) Panel showing representative IF images in continuous sections from EMT6 tumors from mice treated with IV injection with the NPs or saline (control) for 4 h. Tumor hypoxia was determined by pimonidazole binding and HIF-1α antibody. Different stains are from continuous sections of a same tumor: H&E, nucleus (blue), pimonidazole (green), HIF-1α (red). The insets show a representative viable tumor area. Scale bars correspond to 1 mm. Quantification of b) tumor hypoxia and c) HIF-1α after treatments for up to 4 h, determined from classified images (not shown). (n = 3/group). (*) Statistically significant (*p < 0.05) as compared to saline (control) treated groups.

for a week. The in vitro reactivity of the MnO_2 payload and in vivo oxygen generation rate of the hybrid NPs were found to be tunable by modulating the hydrophobicity of matrix material and structure of the hybrid NPs. TMD NPs with higher hydrophilicity and grape-like cluster structure generated oxygen faster than the more hydrophobic and denser LMD NPs, making them a good choice for IT injection. On the other hand, the excellent tumor accumulation and retention as well as lower reactivity especially at the normal pH (pH 7.4) rendered LMD NPs an ideal system for IV treatment. Both hybrid NPs reduced tumor hypoxia and HIF-1α when injected IT, but with different kinetics translatable to hydrophobicity and structure-correlated reactivity rate. When administered IV, LMD NPs were able to effectively decrease hypoxia and HIF-1α in solid tumors. The reactivity of both hybrid NPs increased at acidic pH found in the TME, which was an additional advantage for selective oxygen generation within tumor tissue preventing premature consumption of the MnO_2 payload. This was the first time that MnO_2-containing NPs were specifically designed for IV use and demonstrated safe and effective behavior for the attenuation of tumor hypoxia and HIF-1α through both systemic and local administration. These findings encourage a broader use of hybrid MnO_2 NPs for the modulation of the TME.

4. Experimental Section

Materials: All chemicals were of analytical grade and used without further purification if not indicated otherwise. PMD NPs (<30 nm diameter, zeta potential (ζ) +30 mV) were prepared by strictly following our previous protocol[9] (see the Supporting Information for synthesis details) and were utilized as a precursor for the preparation of hybrid NPs. Graft terpolymer (poly(methacrylic acid)-polysorbate 80-starch) was prepared as previously described without further modifications.[17] Potassium permanganate ($KMnO_4$), poly(allylamine hydrochloride) $\overline{M}_w \approx 15\,000$ (PAH), polyvinyl alcohol (PVA), N-(3-dimethylaminopropyl)-N′-ethylcarbodiimide hydrochloride (EDC), N-hydroxysuccinimide (NHS), N,N′ dicyclohexylcarbodiimidecarbodiimide (DCC), bovine serum albumin (BSA) lyophilized powder, oleic acid, myristic acid, polyoxyethylene (40) stearate, and hydrogen peroxide (H_2O_2) 30 wt% solution were purchased from Sigma-Aldrich (Canada). Myrj 59 polyoxyethylene (100) stearate was from Spectrum Chemicals (USA). Dimethylformamide (DMF) and tetrahydrofuran (THF) were from Caledon (Canada). Indocyanine green (ICG) was purchased from MP Biomedicals (USA). Distilled and deionized (DDI) water were

obtained from a Milli-Q water purifier (Milli-Pore Inc.). Normal saline (0.9% NaCl, pH 5.5) was obtained from sterile IV bags (Baxter Corp, Canada), and the pH was adjusted to 6.8 and 7.4 with 0.1 M HCl and 0.1 M NaOH solutions.

Covalent Conjugation of Oleic Acid to the Surface of PMD NPs (OMD NPs): In a glass vial a DCC solution in DMF (5 mL, 10 mg mL^{-1}) was poured under constant stirring to an oleic acid solution also in DMF (5 mL, 15 mg mL^{-1}), the mixture was left under stirring for 15 min at room temperature (RT), and a PMD aqueous solution (500 µL, 30×10^{-3} M) was then added slowly under vigorous stirring. Big aggregates were observed after 10 min reaction and chloroform (5 mL) was added to clear the dispersion and the mixture was left under stirring overnight at RT. For NP separation, the reaction solution was mixed with acetone in a volume ratio of 1:3 (reaction mixture: acetone), and big aggregates of NPs were formed and then separated by centrifugation (4k rpm, 5 min). The pellet was re-dispersed in chloroform and the washing procedure repeated to remove reaction by products. Finally, the precipitate was redispersed in chloroform and stored at 4 °C.

Preparation TMD NPs: In a first step, terpolymer (50 mg) was dissolved in DDI water (1 mL) and both EDC and NHS (15 mg each) were added and the solution was stirred for 30 min at RT for activation of the carboxylic groups of the TER. Meanwhile, in a 14 mL conical polypropylene tube, PMD NPs (10 mL, 10×10^{-3} M in DDI water) were mixed with a BSA solution (1.2 mL, 10 mg mL^{-1} in normal saline) and Pluronic F-68 solution (50 µL, 100×10^{-3} M in DDI water). The tube was added to a water bath with temperature set to 80 °C and kept under stirring and sonicated for 60 s with an ultrasonic processor probe (100 Hz, 5 mm probe depth, Heischer UP100H, Germany). The mixture was removed from heat, and activated terpolymer (500 µL) was added and the dispersion was sonicated for another 5 min. To obtain NPs with a PEG corona, a mixture of melted polyoxyethylene (40) Stearate (8 mg) and polyoxyethylene (100) Stearate (4 mg) was added during NP preparation prior to adding the crosslinker TER. The obtained brown dispersion was purified by ultracentrifugation (14k rpm, 20 min, 3×) and the pellet was dispersed with 1 mL of sterile saline solution by ultrasonication at RT. It was estimated 85%–90% loading of the PMD NPs occurred in the terpolymer/protein matrix, as determined by measuring remaining PMD NPs in the supernatant, after washing of the NPs, by UV–vis spectrophotometry analysis. A typical preparation led to a $\approx 7 \times 10^{-3}$ M MnO_2 emulsion. TMD NPs were stored at 4 °C and further diluted with cell medium or sterile saline for in vitro and in vivo studies, respectively.

Preparation of LMD NPs: In a 14 mL polypropylene conical tube, PVA (1 mL, 0.1 wt%) was added, and the tube was immersed in a water bath with temperature set to 54 °C. Meanwhile, in a 1.5 mL eppendorf tube myristic acid (7 mg), polyoxyethylene (40) stearate (1 mg), and polyoxyethylenes (100) stearate (2 mg) were dissolved in chloroform (50 µL) and mixed with OMD NPs (50 µL, 75×10^{-3} M) at RT. This mixture was than poured to PVA and sonicated for 3 min with the ultrasonic processor probe (100 Hz, 5 mm probe depth). The obtained emulsion was immediately transferred to ice cold DDI water (0.5 mL) under stirring and gently purged with N_2 for 30 min to remove chloroform. The emulsion was left under low vacuum for 3 h to confirm the complete removal of the organic solvent. It was estimated 100% loading of the OMD NPs occurred in the PEG-lipid matrix, as determined by measuring remaining OMD NPs in the supernatant after ultracentrifugation (14k rpm, 1 h) of the NPs by UV–vis spectrophotometry analysis. A typical preparation led to a $\approx 2.5 \times 10^{-3}$ M MnO_2 emulsion. LMD NPs were stored at 4 °C and further diluted with cell medium or sterile saline for in vitro and in vivo studies, respectively.

Fluorescent NPs: Fluorescent LMD and TMD NPs were obtained by using FITC-labelled myristic acid (see the Supporting Information for synthesis details) and FITC-BSA (Sigma-Aldrich, Canada) for NP preparation, respectively. Near-infrared LMD NPs were obtained by adding an ICG solution (20 µL, 50×10^{-3} M in methanol) to the OMD, myristic acid and polyoxyethylene stearate mixture and NPs were prepared as described above. Near-infrared TMD NPs were obtained also by adding the ICG solution during the NP preparation.

Characterization of the NPs: TEM images were acquired on a Hitachi H7000 electron microscope (Hitachi Canada, Ltd., Canada) with accelerating voltage of 100 kV. NP suspensions in DDI water were placed on carbon-coated grids and dried at RT. A Malvern zeta sizerNano-ZS (Malvern, UK) was used for particle size and zeta potential measurements. NMR measurements were performed in a 400 MHz ^1H NMR spectrometer (Varian Mercury 400, Varian Inc.). Samples were dispersed in deuterated water or in chloroform D in standard NMR tubes and spectra were acquired according to standard proton pulse sequences.

Quenching of H_2O_2: In a small vial NPs (100×10^{-6} M MnO_2) were dispersed in normal saline with pH adjusted to 5.5, 6.8, and 7.4 HCl or NaOH 0.1 M solutions. Hydrogen peroxide (500×10^{-6} M) was added and the residual concentration of H_2O_2 was determined over time using a PeroXOquant assay kit (Pierce, USA), with saline as a vehicle control.

pH Measurements: A pH-sensitive fluorophore SNARF-4F (Life technologies, Cat#: S23920) was used to measure pH changes after NPs reaction with H_2O_2. All necessary calibration curves of the fluorophore were performed following a previously established protocol.[9] The pH changes in the medium were determined after incubation of PMD, TME, and LMD NPs (100×10^{-6} M in saline) with H_2O_2 (500×10^{-6} M) for 1 h at 37 °C (96 well microplate, 200 µL per well). After the required time, SNARF (200×10^{-6} M) was added and fluorescence images of the microplates were recorded at 580 and 640 nm. The fluorescence intensity of each well was obtained by drawing the ROI, and ratio of fluorescence intensities (580/640) was determined. The obtained values were compared with the SNARF calibration curve to determine the pH values of each reaction solution.

Dissolved O_2 (DO) Measurements: O_2 generated by the NPs was measured in a semisealed chamber coupled with a MI-730 microoxygen electrode (Microelectrodes Inc, USA), at 37 °C. PMD, TMD, and LMD NPs (100×10^{-6} M MnO_2) were dispersed in normal saline and dissolved O_2 was removed by bubbling with N_2 for 30 min. H_2O_2 (500×10^{-6} M) was injected into the chamber and generated O_2 was monitored every 60 s using an Oakton pH 1100 (Termo Fisher Scientific Inc, USA) coupled with O_2-ADPT Oxygen Adapter (Microelectrodes Inc, USA). The electrode was calibrated according to manufacturer's instructions. Saline was used as control.

Whole Blood Oxygen Saturation (sO_2) Measurement: Male Sprague Dawley rats (250–300 g, Charles River Laboratories International Inc., USA) were used for blood collection. Blood was collected through terminal cardiac puncture under anesthesia and placed in heparinized tubes (BD Vacutainer) to avoid coagulation. For sO_2 measurements, blood (100 µL) was transferred to a small heparinized tube (Microvette CB 300) and an aliquot of NPs (PMD, TMD, and LMD) and hydrogen peroxide stock solution were added to make the MnO_2 and H_2O_2 concentration in the blood 100×10^{-6} and 500×10^{-6} M, respectively. Saline was used as control. Samples were incubated at 37 °C and 5% CO_2 for 1 h prior to imaging. In vitro PA imaging of sO_2 in a phantom was performed using a Vevo 2100 LAZR PA imaging system (FUJIFILM VisualSonics Inc., Canada) with a 21 MHz-centered transducer. Samples were passed through polyethylene tubes that were submerged in water. Using laser wavelengths of 750 and 850 nm, sO_2 was calculated by a built-in software based on the difference in the received photoacoustic signals at the two wavelengths.

Cancer Cell Lines: Murine EMT6 and human MDA-MB-231 breast cancer cell lines were utilized and cultured following standard cell culture procedures.[17a] For all in vitro experiments, cells in αMEM medium (10^5 cells per mL) were treated with NPs for 48 h and cell viability was measured using a standard MTT protocol after 48 h.[17a]

Cellular Uptake of NPs: Murine EMT6 and human MDA-MB-231 breast tumor cells (10^5 cells, 96 well plate) were incubated for 1 h with fluorescent TMD and LMD NPs (100×10^{-3} M) at 37 °C before microscopic analysis. A laser scanning confocal microscope (Zeiss LSM510, Canada) was used to image live cells. Cell nuclei were stained blue with Hoechst 33342 (Invitrogen, Cat#: H3570).

Animal Models: Female Balb/c mice (8–10 week old, Jackson Laboratories, USA) were used for in vivo experiments using a xenograft

tumor model previously established in our laboratory.[19] Solid tumors of murine EMT6 breast cancer cells (10^6) were grown orthotopically in Balb/c mice and animals were randomly allocated for all treatments (n = 3/group). For IT experiments, tumors were injected with TMD or LMD NPs solution in saline (50 μL, 1×10^{-3} M). For IV experiments, mice received a tail vein injection of NP solution in saline (200 μL, 1×10^{-3} M). Controls were treated with equivalent volume of saline. For experiments with rats, male Sprague Dawley rats (250–300 g, Charles River Laboratories International Inc., USA) were used. All animal procedures were strictly complied with the ethical and legal requirements under Ontario's Animals for Research Act and the Federal Canadian Council on Animal Care guidelines for the care and use of laboratory animals and were approved by the University Animal Care Committee of the University of Toronto and University Health Network animal care committee.

Hepatotoxicity of NPs: Hepatocyte extraction and preparation and the assays to determine hepatocyte viability, ROS formation, and MMP were performed as previously described without further modifications.[26] Suspended hepatocytes isolated from rat liver (10^6 cells per mL, 10 mL) were incubated with PMD, TMD, or LMD NPs dispersed in culture medium at desired concentrations (i.e., 100×10^{-6} and 400×10^{-6} M) and incubated for 2 h at 37 °C. Cell viability was assayed with trypan blue exclusion test. ROS formation was determined by measuring the fluorescence intensity of dichlorofluorescin diacetate added to aliquots of the hepatocytes. MMP was determined by measuring the uptake of rhodamine 123 by the hepatocytes.

In Vivo Biodistribution of NPs: A Xenogen IVIS Spectrum Imaging System (Caliper Life Sciences Inc., USA) was used to image EMT6 tumor bearing Balb/c mice over time following IV injection with near-infrared labeled TMD or LMD NPs. At each time point, a bright field image was acquired and fluorescence-labeled NPs were imaged at 754 nm excitation and 820 nm emission. Fluorescence images were quantified by equalizing the fluorescence intensity range across all images. For ex vivo imaging of the organs, mice were euthanized 4 h and 24 h post NP injections, and organs were resected and imaged as described above.

Immunohistochemistry and Immunofluorescence: EMT6 Balb/c tumor bearing mice (n = 3/group) were treated IT or IV with NPs (TMD or LMD) or saline (control). After predetermined times, animals received an intraperitoneal injection of pimonidazole HCl solution (60 mg kg^{-1}) (Hypoxyprobe-1 plus kit, HypoxyprobeInc), and were sacrificed 30 min after pimonidazole administration. Tumor tissues were quickly harvested, formalin fixed, then embedded in paraffin. Separate sections were stained with H&E. For detection of pimonidazole, sections were incubated with mouse FITC-conjugated anti-pimonidazole antibody and rabbit anti-FITC rabbit secondary antibody (dilution 1:100, Hypoxyprobe-1 plus kit, HypoxyprobeInc) following the kit's instructions. Staining for HIF-1α was done by incubation with Rabbit polyclonoal HIF-1α antibody (dilution 1:100, Novus Biologicals, Cat#: NB100–134), secondary goat anti-rabbit HIF-1α biotin conjugated (dilution 1:200, Vector Labs, Cat#: BA-1000), and Alexa 594 conjugated streptavidin (dilution 1:1000, Invitrogen, Cat#: S-32356). Nuclei were stained with DAPI (dilution 1:5000, Invitrogen, catalog number: D1306). Slides were mounted in Vectashield mounting medium (Vector Labs, Cat#: h-1000). Tumor tissue preparation and staining were performed by the CMHD Pathology Core laboratory at Mount Sinai Hospital, Toronto.

Image Acquisition and Analysis: Slides were scanned with a NanoZoomer 2.0 RS whole slide scanner (Hamamatsu, Japan). Images of the three channels (red, green, and blue) were obtained with NPD.view2 software (Hamamatsu, Japan). Image intensity quantification was performed with ImageJ software (NIH, USA) by converting channels to binary images. Thresholds for the fluorescent signals were interactively set above the background for each marker, and images were colored coded for visual evaluation. H&E sections were utilized as a guide to delineate viable tumor areas. Nontumor tissue (including lymph nodes), necrotic areas and artefacts were carefully excluded. The positive area (%) was defined as the viable tumor area positive for the marker, divided by the total viable tumor area.

Statistical Analysis: Data are presented as mean ± standard deviation of the mean (SEM) for results obtained from three independent trials unless otherwise indicated. Student's t-test or analysis of variance (ANOVA) followed by Tukey t-test (OriginPro8) were utilized to determine statistical significance between two or more groups, respectively. p-values < 0.05 were considered statistically significant.

Supporting Information

Supporting Information is available from the Wiley Online Library or from the author.

Acknowledgements

C.R.G. and A.Z.A. contributed equally to this work. This work was financially supported in part by grants from the Natural Sciences and Engineering Research Council (NSERC) of Canada (2013–2018 – #RGPIN 170460–08) to X.Y.W. and the Canadian Cancer Society Innovation Grant (2013–2015, Grant No. 702133) to X.Y.W., R.S.D., and A.M.R. We also acknowledge Dr. Hibret Adissu pathologist from the CMHD Pathology Core Laboratory at Mount Sinai Hospital, Toronto, Canada, for the assistance with histology analysis.

Received: December 19, 2014
Revised: January 19, 2015
Published online: February 18, 2015

[1] a) S. Masuda, J. C. I. Belmonte, *Nat. Rev. Clin. Oncol.* **2012**, *10*, 79; b) M. Milosevic, P. Warde, C. Ménard, P. Chung, A. Toi, A. Ishkanian, M. McLean, M. Pintilie, J. Sykes, M. Gospodarowicz, C. Catton, R. P. Hill, R. G. Bristow, *Clin. Cancer Res.* **2012**, *18*, 2108; c) O. Trédan, C. M. Galmarini, K. Patel, I. F. Tannock, *J. Natl. Cancer Inst.* **2007**, *99*, 1441; d) R. G. Bristow, R. P. Hill, *Nat. Rev. Cancer.* **2008**, *8*, 180.

[2] M. Mimeault, S. K. Batra, *J. Cell. Mol. Med.* **2013**, *17*, 30.

[3] a) J. M. Brown, A. J. Giaccia, *Cancer Res.* **1998**, *58*, 1408; b) R. A. Gatenby, R. J. Gillies, *Nat. Rev. Cancer.* **2008**, *8*, 56; c) N. C. Denko, *Nature Rev. Cancer.* **2008**, *8*, 705; d) A. S. Ljungkvist, J. Bussink, J. H. Kaanders, N. E. Wiedenmann, R. Vlasman, A. J. van der Kogel, *Radiat. Res.* **2006**, *165*, 326.

[4] R. A. Cairns, I. S. Harris, T. W. Wak, *Nat. Rev. Cancer.* **2011**, *11*, 85.

[5] J. Chiche, M. C. Brahimi-Horn, J. Pouyssegur, *J. Cell Mol. Med.* **2010**, *14*, 771.

[6] a) J. W. Wojtkowiak, D. Verduzco, K. J. Schramm, R. Gillies, *Mol. Pharm.* **2011**, *8*, 2032; b) I. F. Robey, L. A. Nesbit, *Biomed. Res. Int.* **2013**, *2013*, 485196; c) W. Wu, Q. Yang, T. Li, P. Zhang, R. Zhou, C. Yang, *Artif. Cells Blood Substit. Immobil. Biotechnol.* **2009**, *37*, 163; d) R. Cavalli, A. K. Akhter, A. Bisazza, P. Giustetto, F. Trotta, P. Vavia, *Int. J. Pharm.* **2010**, *402*, 254; e) D. L. Nielsen, M. Andersson, J. L. Andersen, C. C. Kamby, *Breast Cancer Res.* **2010**, *12*, 209; f) A. D. Wagner, C. Thomssen, J. Haerting, S. Unverzagt, *Cochrane Database Syst. Rev.* **2012**, *11*, CD008941; g) Y. J. Kim, H. J. Lee, T. M. Kim, T. S. Eisinger-Mathason, A. Y. Zhang, B. Schmidt, D. L. Karl, M. S. Nakazawa, P. J. Park, M. C. Simon, S. S. Yoon, *Int. J. Cancer.* **2013**, *132*, 29.

[7] a) E. Fokas, W. G. McKenna, R. J. Muschel, *Cancer Metastasis Rev.* **2012**, *31*, 823; b) J. Karar, A. Maity, *Cancer Biol Ther.* **2008**, *8*, 1994; c) S. Rockwell, I. T. Dobrucki, E. Y. Kim, S. T. Marrison, V. T. Vu, *Curr. Mol. Med.* **2009**, *9*, 442; d) E. T. Shinohara, A. Maity, *Curr. Mol. Med.* **2009**, *9*, 1034; e) D. Kwatra, A. Venugopal, S. Anant, *Transl.*

Cancer Res. **2013**, *2*, 320; f) A. Pottier, E. Borghi, L. Levy, *Anticancer Res.* **2014**, *34*, 443.

[8] a) A. Rapisarda, G. Melillo, *Nat. Rev. Clin. Oncol.* **2012**, *24*, 378; b) J. N. Bottsford-Miller, R. L. Coleman, A. K. Sood, *J. Clin. Oncol.* **2012**, *10*, 4026; c) H. J. Park, R. J. Griffin, S. Hui, S. H. Levitta, C. W. Songa, *Radiat. Res.* **2012**, *177*, 311.

[9] P. Prasad, C. R. Gordijo, A. Z. Abbasi, A. Ip, A. Maeda, A. M. Rauth, R. S. DaCosta, X. Y. Wu, *ACS Nano* **2014**, *8*, 3202.

[10] M. Bradley, J. R. B. Tebo, B. G. Clement, G. J. Dick, K. J. Murray, D. Parker, R. Verity, S. M. Webb, *Annu. Rev. Earth Pl. Sc.* **2004**, *32*, 287.

[11] a) C. R. Gordijo, A. J. Shuhendler, X. Y. Wu, *Adv. Funct. Mater.* **2010**, *20*, 1404; b) C. R. Gordijo, K. Koulajian, A. J. Shuhendler, L. D. Bonifacio, H. Y. Huang, S. Chiang, G. A. Ozin, A. Giacca, X. Y. Wu, *Adv. Funct. Mater.* **2011**, *21*, 73.

[12] X. L. Luo, J. J. Xu, W. Zhao, H. Y. Chen, *Biosens. Biolectron.* **2004**, *19*, 1295.

[13] L. Yildirimer, N. T. K. Thanh, M. Loizidou, A. M. Seifalian, *Nano Today* **2011**, *6*, 585.

[14] M. A. Hasan, M. I. Zaki, L. Pasupulety, K. Kumari, *Appl. Catal. A- Gen.* **1999**, *181*, 171.

[15] a) S. L. Brock, N. Duan, Z. R. Tian, O. Giraldo, H. Zhou, S. L. Suib, *Chem. Mater.* **1998**, *10*, 2619; b) J. Cabana, L. Monconduit, D. Larcher, M. R. Palacín, *Adv. Mater.* **2010**, *22*, E170; c) W. Wei, X. Cui, W. Chen, D. Ivey, *Chem. Soc. Rev.* **2011**,*40*, 1697; d) D. Koziej, A. Lauria, M. Niederberger, *Adv. Mater.* **2014**, *26*, 235.

[16] a) M. J. Sailor, J.-H. Park, *Adv. Mater.* **2012**, *24*, 3779; b) N. Sanvicens, M. P. Marco, *Trends Biotechnol.* **2008**, *26*, 425; c) S. R. MacEwan, D. J. Callahan, A. Chilkoti, *Nanomedicine* **2010**, *5*, 793; d) R. A. Petros, J. M. DeSimone, *Nat. Rev. Drug Discov.* **2010**, *9*, 615.

[17] a) A. Shalviri, G. Raval, P. Prasad, C. Chan, Q. Liu, H. Heerklotz, A. M. Rauth, X. Y. Wu, *Eur. J. Pharm. Biopharm.* **2012**, *82*, 587; b) A. Shalviri, H. K. Chan, G. Raval, M. J. Abdekhodaie, Q. Liu, H. Heerklotz, X. Y. Wu, *Colloids Surf. B Biointerfaces.* **2013**, *1101*, 405; c) A. Shalviri, W. D. Foltz, P. Cai, A. M. Rauth, X. Y. Wu, *J. Control. Release* **2013**, *167*, 11; d) J. Li, P. Cai, A. Shalviri, J. T. Henderson, C. He, W. D. Foltz, P. Prasad, P. M. Brodersen, Y. Chen, R. DaCosta, A. M. Rauth, X. Y. Wu, *ACS Nano* **2014**, *28*, 9925.

[18] a) H. L. Wong, R. Bendayan, A. M. Rauth, Y. Li, X. Y. Wu, *Adv. Drug Deliv. Rev.* **2007**, *59*, 491; b) H. L. Wong, R. Bendayan, A. M. Rauth, H. Y. Xue, K. Babakhanian, X. Y. Wu, *J. Pharmacol Exp. Ther.* **2006**, *317*, 1372; c) H. L. Wong, A. M. Rauth, R. Bendayan, J. L. Manias, M. Ramaswamy, Z. Liu, S. Z. Erhan, X. Y. Wu, *Pharm. Res.* **2006**, *23*, 1574; d) H. L. Wong, R. Bendayan, A. M. Rauth, X. Y. Wu, *J. Pharm. Sci.* **2004**, *93*, 1993; e) H. L. Wong, A. M. Rauth, R. Bendayan, X. Y. Wu, *J. Control Release.* **2006**, *116*, 275.

[19] a) A. J. Shuhendler, P. Prasad, R. X. Zhang, M. A. Amini, M. Sun, P. P. Liu, R. G. Bristow, A. M. Rauth, X. Y. Wu, *Mol Pharm.* **2014**, *11*, 2659; b) A. J. Shuhendler, P. Prasad, P. Cai, K. K. Hui, J. T. Henderson, A. M. Rauth, X. Y. Wu, *Nanomed. Nanotechnol.* **2013**, *9*, 795; c) A. J. Shuhendler, P. Prasad, M. Leung, A. M. Rauth, R. S. Dacosta, X. Y. Wu, *Adv. Healthcare Mater.* **2012**, *1*, 600; d) P. Prasad, A. Shuhendler, P. Cai, A. M. Rauth, X. Y. Wu, *Cancer Lett.* **2013**, *334*, 263.

[20] H. F. Zhang, K. Maslov, G. Stoica, L. V. Wang, *Nat. Biotech.* **2006**, *34*, 848.

[21] B. Halliwell, M. V. Clement, L. H. Long, *FEBS Lett.* **2000**, *486*, 10.

[22] a) H. Yuan, J. Miao, Y. Z. Du, J. You, F. Q. Hu, S. Zeng, *Int. J. Pharm.* **2008**, *348*, 137; b) K. Teskac, J. Kristl, *Int. J. Pharm.* **2010**, *390*, 61.

[23] a) W. H. De Jong, P. J. Borm, *Int. J. Nanomedicine.* **2008**, *3*, 133; b) A. M. Nystrom, B. Fadeel, *J. Control. Release* **2012**, *161*, 403.

[24] a) Y. M. Jeon, W. J. Kim, M. Y. Lee, *J. Environ. Biol.* **2013**, *34*, 283; b) J. W. Yoo, E. Mitragotri, S. Factors, *Curr. Pharm. Des.* **2010**, *16*, 2298.

[25] S. P. Singh, M. Kumari, S. I. Kumari, M. F. Rahman, M. Mahboob, P. Grover, *J. Appl. Toxicol.* **2013**, *33*, 1165.

[26] A. A. Maruf, L. Wan, P. J. O'Brien, *Biomed. Res. Int.* **2014**, *2014*, 379748.

[27] a) Y. Li, X. Tian, Z. Lu, C. Yang, G. Yang, X. Zhou, H. Yao, Z. Zhu, Z. Xi, X. Yang, *J. Nanosci. Nanotechnol.* **2010**, *10*, 397; b) J. Wang, X. Deng, F. Zhang, D. Chen, W. Ding, *Nanoscale Res. Lett.* **2014**, *9*, 117. c) C. Xue, J. Wu, F. Lan, W. Liu, X. Yang, F. Zeng, H. Xu, *J. Nanosci. Nanotechnol.* **2010**, *10*, 8500.

[28] J. Lazarovits, Y. Y. Chen, E. A. Sykes, W. C. W. Chan, *Chem. Commun.* **2014**, *51*, 2756.

[29] a) S. E. Rademakers, J. Lok, A. J. van der Kogel, J. Bussink, J. H. Kaanders, *BCC Cancer.* **2011**, *11*, 167; b) A. W. Mailloux, M. R. I. Young, *J. Immunol.* **2009**, *182*, 2753.

[30] a) S. Rockwell, *Br. J. Cancer Suppl.* **1978**, *3*, 212; b) Y. Shibamoto, K. Ono, M. Takahashi, E. Kano, H. Hori, T. Shibata, S. Inayama, M. Abe, *Jpn. J. Cancer Res.* **1986**, *77*, 1027; c) M. Oita, Y. Uto, M. Tominaga, M. Sasaki, Y. Hara, T. Kishi, H. Hori, *Anticancer Res.* **2014**, *34*, 4621.

[31] a) C. R. Taylor, R. M. Levenson, *Histopathology* **2006**, *49*, 411; b) L. L. Matos, D. C. Trufelli, M. G. de Matos, M. A. da Silva Pinhal, *Biomark Insights* **2010**, *9*, 9.